Spatially Resolved Analysis of Light-Induced Degradation Effects on LBIC in Multicrystalline Silicon Solar Cells

Selma Aouida

Laboratoire de PhotoVoltaïque, Centre de Recherches et des Technologies de l'Energie, Technopôle de Borj-Cédria, BP 95 Hammam-Lif, 2050 Tunis, Tunisie

Abstract

Light-induced degradation (LID) in silicon solar cells is one of the primary degradation mechanisms that reduces the efficiency of photovoltaic cells and modules, typically causing a performance loss of up to 10% within the first few hours of operation. This degradation is mainly attributed to the formation of boron-oxygen (B-O) complexes under sunlight exposure, which act as recombination centers and reduce the minority carrier lifetime. This study investigates the impact of LID on the photocurrent of a multicrystalline silicon solar cell generated by laser excitation at various wavelengths (985 nm, 950 nm, 878 nm, and 657 nm). This approach enables spatially resolved analysis of the LID effect across the solar cell, with laser penetration depths ranging from 2 µm to 80 µm. Our experimental results show that the degradation is more pronounced in the bulk region of the solar cell, with the photocurrent reduction reaching up to 50 µA at 985 nm and decreasing to 40 µA at 657 nm. The study of the internal and external quantum efficiency of multicrystalline silicon solar cells reveals that a degradation of ~10%-15% occurs across all wavelengths, suggesting that degradation mechanisms affect carrier collection homogeneously.

Keywords: LID, LBIC, silicon solar cells, Semilab WT 2000 PVN, IQE, EQE

1. Introduction

Silicon-based solar cells dominate the photovoltaic market due to their reliability and mature fabrication processes. However, their performance degradation under illumination remains a critical challenge for long-term energy yield [1-3]. Light-induced degradation (LID), primarily caused by boron-oxygen (B-O) complexes or metal impurities in p-type silicon, results in a significant drop in conversion efficiency, up to 10% in severe cases [4]. While bulk LID effects are well-documented [5], spatially resolved analyses linking LID to local charge carrier dynamics are scarce. Conventional methods, such as IV curves, overlook microscopic heterogeneities, thereby masking critical defect-related mechanisms. A combination of Laser Beam-Induced Current (LBIC) and reflectance mapping techniques is employed to extract spatial distributions of External Quantum Efficiency (EQE), Internal Quantum Efficiency (IQE), and carrier diffusion length before and after LID activation. This approach enables a detailed analysis of defect behavior and its effect on carrier transport properties, contributing to a better understanding of LID phenomena and their mitigation in industrial solar cell production.

We hypothesize that LID-induced defects create localized recombination centers, disproportionately reducing LBIC in specific regions. To test this, we employ high-resolution LBIC mapping before and after

LID activation on a multicrystalline silicon solar cell. This work presents quantitative, spatially resolved experimental results of LID impacts on LBIC, providing insights for targeted defect passivation strategies.

2. Experimental

2.1 Sample preparation

This study employs a commercially available p-type multicrystalline silicon solar cell. Two distinct states of the cell are investigated: before and after LID-activation. Measurements are first achieved on the solar cell without LID. After that, the LID activation is performed by exposing the device to continuous illumination using a halogen lamp for 90 hours; this duration is presumed sufficient to activate LID defects [6]. Following this stress period, measurements are conducted on the LID-activated state.

2.2 Measurement details

The measurements were conducted using a Semilab WT-2000 PVN system, which enables Laser Beam-Induced Current (**LBIC**) and reflectance (**R**) mapping across multiple laser wavelengths on photovoltaic (PV) cells. A laser beam of defined photon flux (φ) and energy is directed onto the cell, inducing a localized photocurrent measured as the short-circuit current (**I_{sc}).**

The system operates with laser wavelengths of 984 nm, 950 nm, 878 nm, and 657 nm, corresponding to penetration depths (α) of 78 µm, 45 µm, 18 µm, and 2.5 µm, respectively. For each wavelength, the External Quantum Efficiency (**EQE**) is determined according to:

$$\mathbf{QE} = \frac{\mathbf{I_{Electron}}}{\mathbf{I_{Photon}}} \ \textbf{(Eq. 1)}$$

I_{photon} is the incident photon energy, and **$I_{electron}$** is the induced electron current of the solar cell.

Reflectance (**R**) maps acquired during the measurement process allow for the calculation of the Internal Quantum Efficiency (**IQE**), using the relation:

$$\mathbf{IQE} = \frac{\mathbf{EQE}}{\mathbf{(1-R)}} \ \textbf{(Eq. 2)}$$

A plot of 1/IQE versus 1/α yields a linear relationship. The intercept with the x-axis corresponds to the minority carrier diffusion length. Based on certain assumptions, the relationship can be expressed as:

$$\frac{\mathbf{1}}{\mathbf{IQE}} = \mathbf{C} * \left(\mathbf{L_D} + \frac{\mathbf{1}}{\boldsymbol{\alpha}}\right) \ \textbf{(Eq. 3)}$$

where **C** is a constant and **L_D** denotes the diffusion length.

The Semilab WT-2000 PVN system thus provides spatially resolved **EQE** and **IQE** maps for each laser wavelength, enabling the extraction of diffusion length distributions and corresponding carrier lifetimes across the PV device.

3. Results and discussions

Figure 1 presents the LBIC mapping of the four lasers and the corresponding histograms before and after LID activation. The obtained maps of the studied solar cell, acquired at a resolution of 250 µm on more than 4 cm^2, clearly reveal the front metallization pattern, including the current-collecting fingers and busbar, which exhibit lower photocurrent values due to shading effects. Additionally, the spatial distribution of grain boundaries (GBs) within the multi-crystalline silicon structure is discernible, appearing as interconnected lines where carrier recombination reduces the local current response.

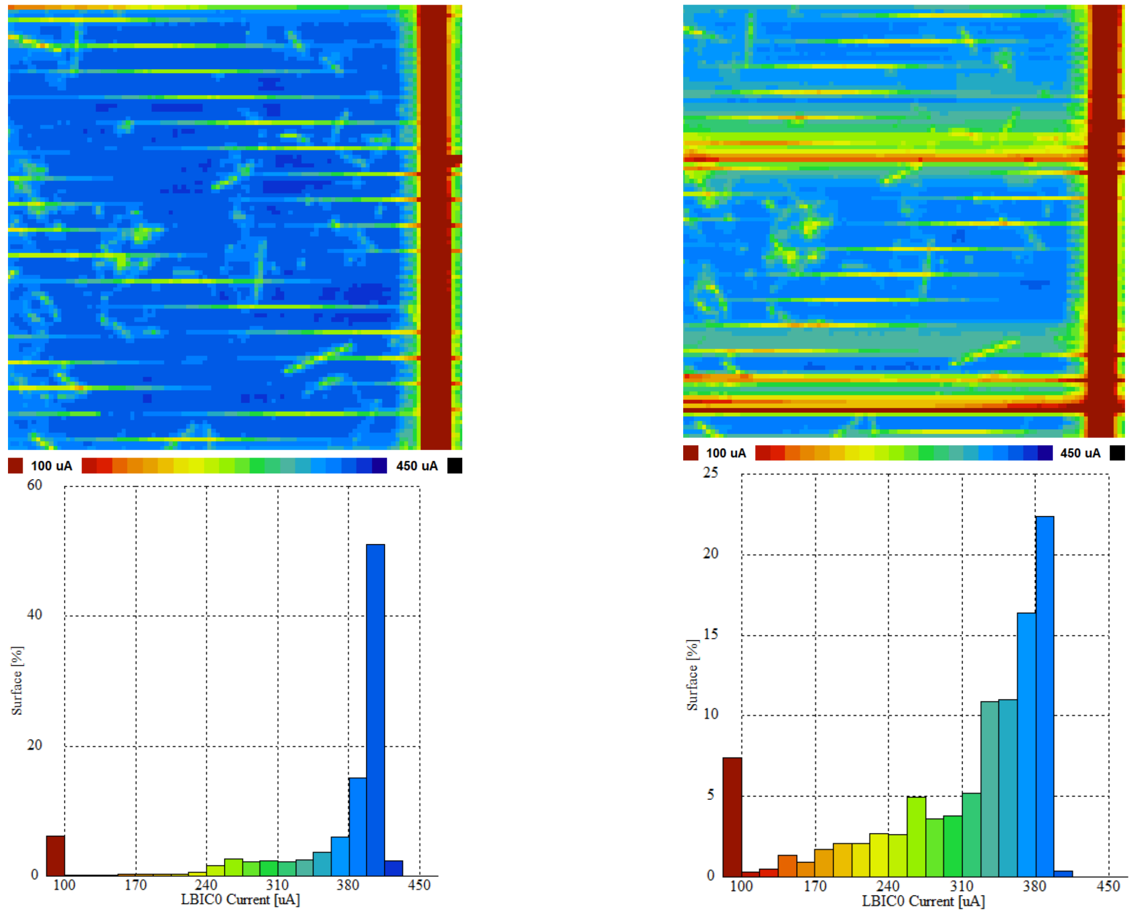

Before LID activation

After LID activation, 90-hour halogen lamp irradiation

984 nm-LBIC

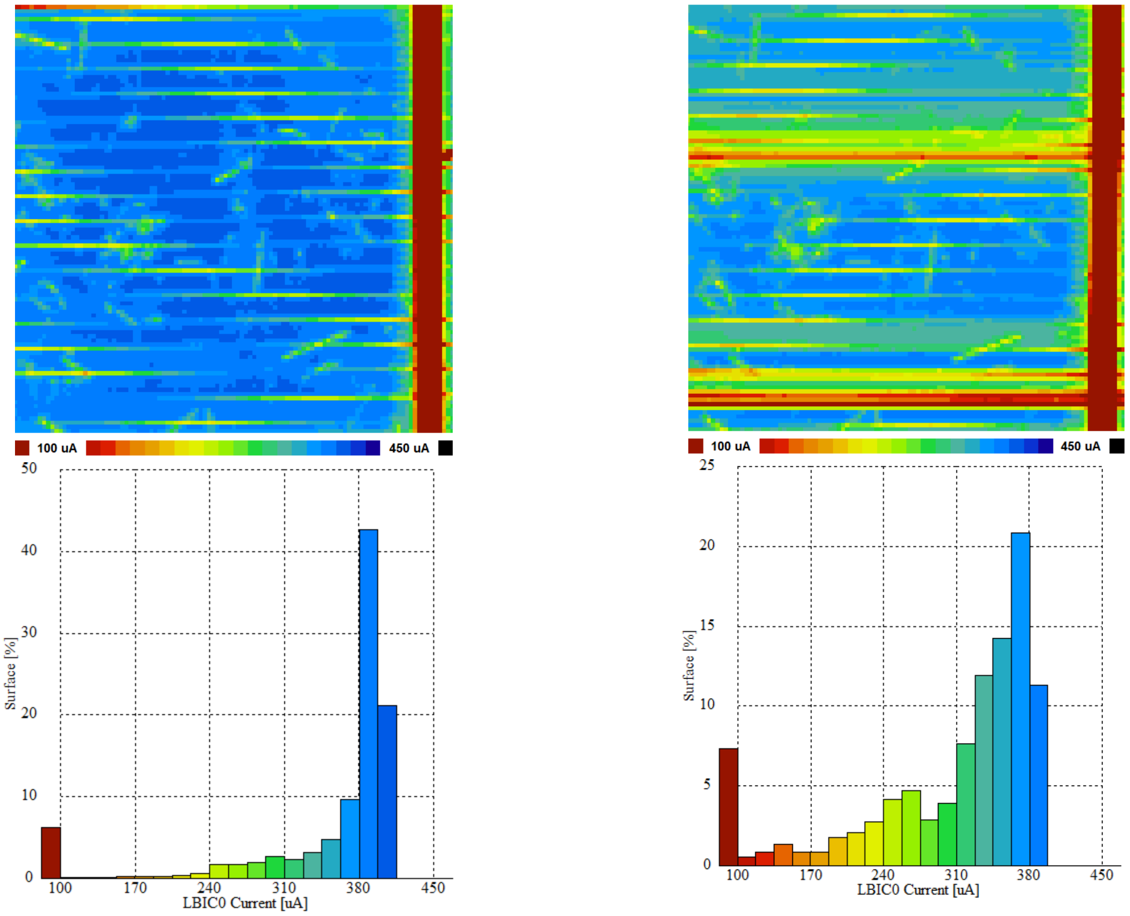

950 nm –LBIC

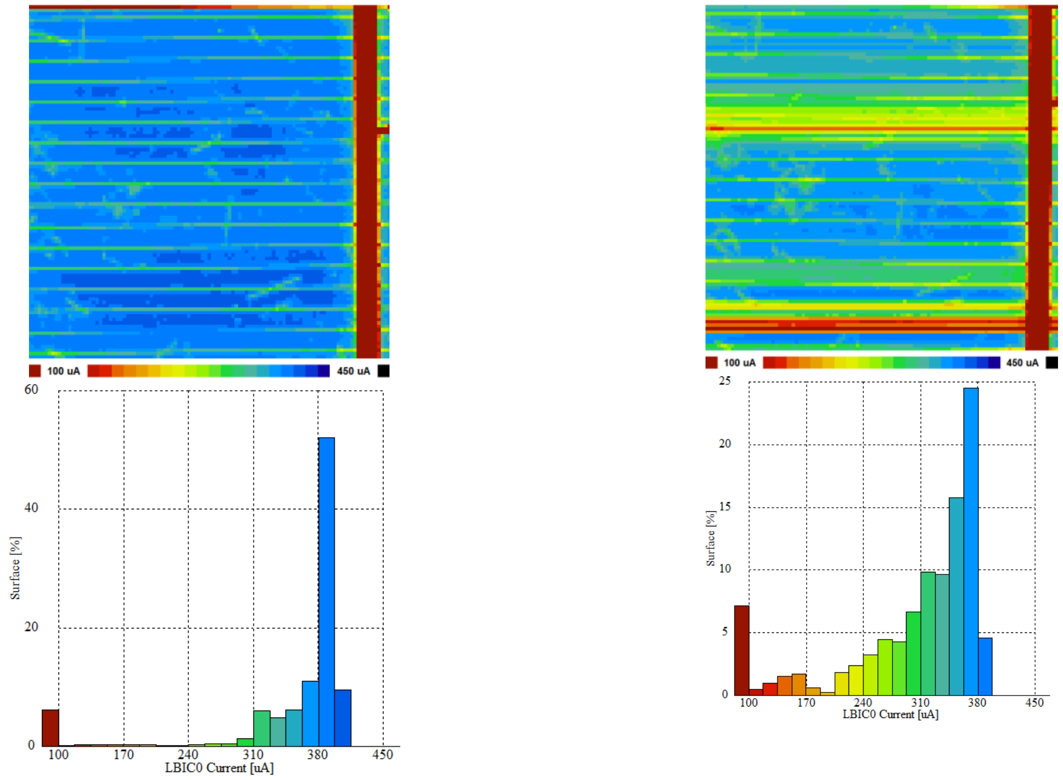

878 nm- LBIC

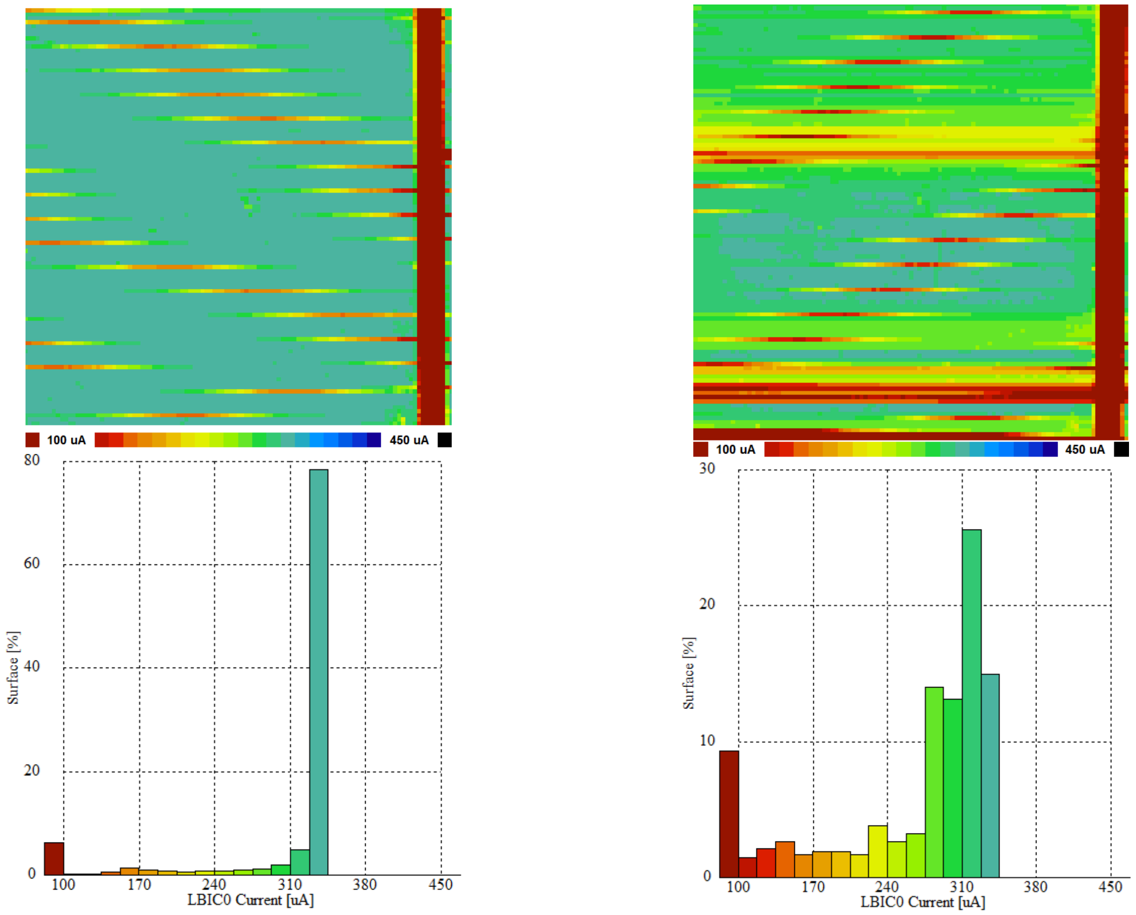

657 nm LBIC

Figure 1: λ - LBIC mapping and the corresponding histograms before and after LID activation

3.1 Light penetration depth-dependent LID effect on LBIC

Figure 2 displays the histograms of wavelength-dependent light-induced current (λ-LBIC) maps acquired before (A) and after (B) LID activation. Analysis of the pre-degradation state (A) reveals that approximately 6% of the cell surface area is shadowed by the metallic front contact grid, exhibiting current values below 100 µA. The photogenerated current shows strong wavelength dependence, with the 657 nm (penetration depth ~2 µm) yielding a uniform response of ~327 µA across 78% of the active surface, indicating minimal influence from grain boundaries in the heavily doped emitter region. For longer wavelengths (878 nm, 950 nm, and 984 nm, with respective penetration depths of ~18 µm, 45 µm, and 78 µm), the maximum current progressively increases to 397 µA (peak distribution at 380 µA) and 415 µA (~50% of surface at 397 µA), reflecting enhanced carrier generation in deeper regions. The spatial non-uniformity observed at these wavelengths directly correlates with recombination activity at multicrystalline grain boundaries, as resolved in the LBIC maps. This wavelength-dependent behavior systematically illustrates how carrier collection efficiency varies with probing depth and is influenced by bulk recombination processes.

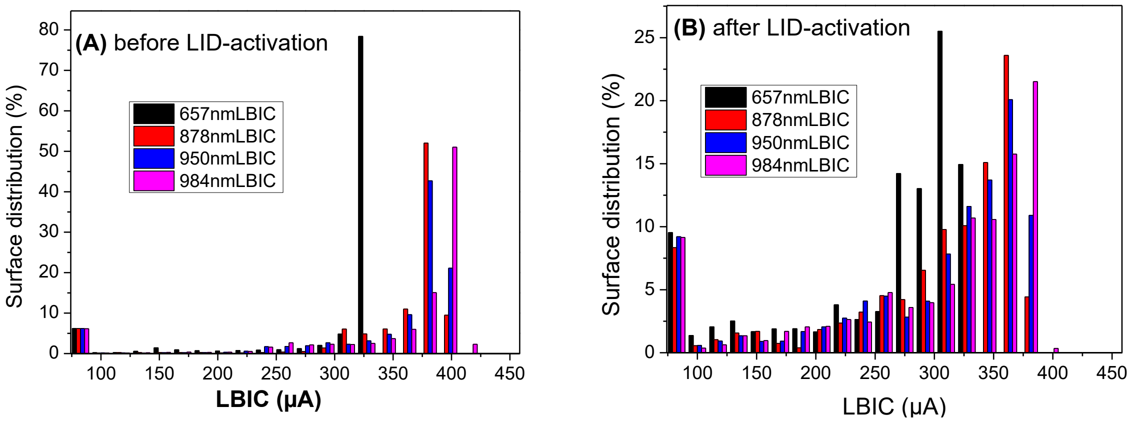

Figure 2 : Histograms of λ-LBIC maps before (A) and after (B) LID-activation

After 90 hours of continuous illumination to activate LID [6, 7], the LBIC distribution exhibited notable changes, with an increased surface distribution of values around 100 µA and 300 µA and a reduction in maximum LBIC values. As summarized in Table 1, before LID activation, the solar cell demonstrated a maximum LBIC of 327 µA under 657 nm laser illumination, with 15% of the cell area remaining unaffected even after prolonged exposure. However, for longer wavelengths (878 nm, 950 nm, and 984 nm), which probe deeper into the bulk, the maximum LBIC values decreased by approximately 17 µA. The average LBIC values, which include contributions from contact regions, declined by ~40 µA at 657 nm and ~50 µA for the deeper-penetrating wavelengths. These results indicate that the LID effect is more pronounced in the bulk regions of the solar cell, suggesting a depth-dependent degradation mechanism. The degradation at longer wavelengths indicates that LID predominantly affects bulk areas, consistent with the known role of boron-oxygen (BO) defect activation in Czochralski (Cz) silicon [2, 8-10]. The stability at 657 nm suggests that surface and near-surface regions, where carrier generation is concentrated for shorter wavelengths, may be partially shielded by effective passivation layers [11]. However, the ~40 µA drop in average LBIC at this wavelength implies additional contributions from contact degradation or increased series resistance, as reported in cases of prolonged illumination-induced metal contact deterioration [12]. The 657 nm-LBIC map after illumination (Figure 1) presents a significant decrease in measured current around contact fingers.

Wavelength λ (nm)	**LBIC before LID-activation**			**LBIC after LID-activation**		
	Maximum Value	Surface (%)	Average	Maximum Value	Surface (%)	Average
657	327 µA	78%	306 µA	327 µA	15%	263 µA
878	397 µA	10%	350 µA	380 µA	4%	301 µA
950	397 µA	21%	351 µA	380 µA	10%	301 µA
984	415 µA	2%	357 µA	397 µA	0.3%	307 µA

Table 1: λ-LBIC values before and after LID activation

3.2 Wavelength-dependent LID effect on EQE and IQE

In this section, to mitigate contact-induced artifacts, particularly near the busbar, the analysis is restricted to a circular region (radius = 10 mm). By tracking the grain boundary (GB) response, we ensure consistent spatial comparison of the solar cell's surface before and after light-induced degradation (LID) activation. Figure 3 displays the spectral EQE (λ-EQE) distributions under both conditions. Figure 4 presents λ-EQE and λ-IQE maps before and after LID activation in the investigated region. We note that the peak of EQE reaches 98% at 657 nm, with an average of 96.6% across >80% of the analyzed area (Figure 3). The corresponding IQE rises to 98.6% (Table 2), demonstrating near-unity charge collection efficiency for shallowly absorbed photons. At longer wavelengths, the EQE declines to 88.8% (878 nm), 82.2% (950 nm), and 75.8% (984 nm), attributed to increasing carrier generation depth. Notably, the IQE values for these wavelengths are ~6% higher (Table 2), implicating surface reflectance—rather than bulk recombination—as the primary limiting factor.

After LID activation, a reduction of ~10%-15% in both EQE and IQE occurs across all wavelengths, suggesting degradation mechanisms that affect carrier collection homogeneously (Table 2). The high pre-LID efficiencies, particularly at 657 nm, reflect optimal emitter passivation and minority-carrier extraction. In contrast, the lower performance at near-infrared wavelengths highlights the compounding effects of bulk recombination (e.g., at GBs) and transport losses. The consistent 6% IQE-EQE disparity further highlights the role of parasitic absorption and reflection losses for photons with deeper penetration (Table 2).

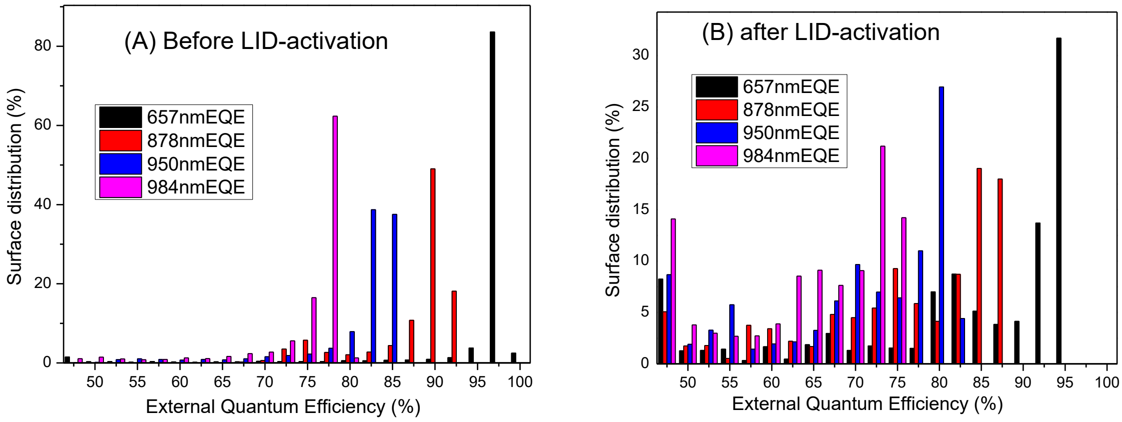

Figure 3 : Histograms of λ-EQE maps before (A) and after (B) LID-activation

Wavelength λ (nm)	Average EQE (%)		Average IQE (%)	
	Before LID-activation	After LID-activation	Before LID-activation	After LID-activation
657	96.6 %	82%	98.6 %	83%
878	88.8 %	76%	94.3%	79%
950	82.2 %	70%	88.3 %	75%
984	75.8 %	64%	82.3 %	69%

Table 2: Average EQE and IQE values before and after LID-activation

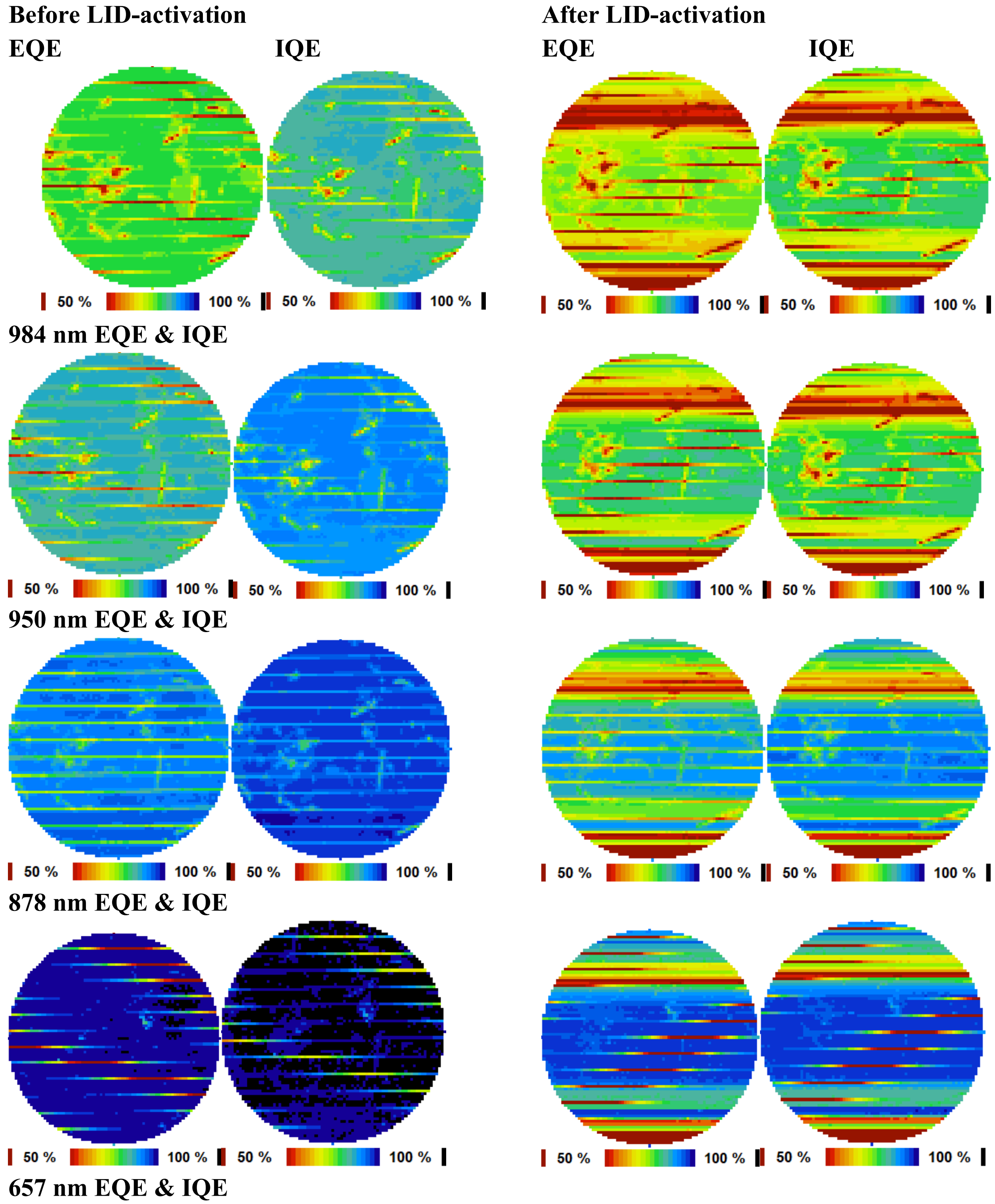

Figure 4 : λ-EQE and λ-IQE maps of the multi-crystalline silicon solar cell before and after LID activation

3.3 LID effect on minority carrier diffusion length and lifetime

The obtained internal quantum efficiency (IQE) maps correlated with reflection maps, enable the determination of minority carrier diffusion length (L) distributions across the solar cell before and after LID activation, as derived from Eq. (3). Furthermore, the diffusion length maps can be converted into minority carrier lifetime (τ) maps using the relation $L = \sqrt{(D\tau)}$, where D is the diffusivity. Figure 5 presents these spatial distributions along with their corresponding average values. Following LID activation, the average minority carrier diffusion length decreases from 451 µm to 393 µm, while the minority carrier lifetime drops from 69 µs to 55 µs, indicating a measurable degradation in carrier transport properties. This degradation suggests a significant deterioration in bulk carrier transport properties, likely attributable to defect activation or increased recombination centers. The stronger reduction in τ compared to L may indicate enhanced Shockley-Read-Hall (SRH) recombination [13, 14], as lifetime is more sensitive to defect density than diffusivity. These findings underscore the impact of LID on the solar cell performance.

Before LID activation **After LID activation**

Monority carrier diffusion length LD (µm)

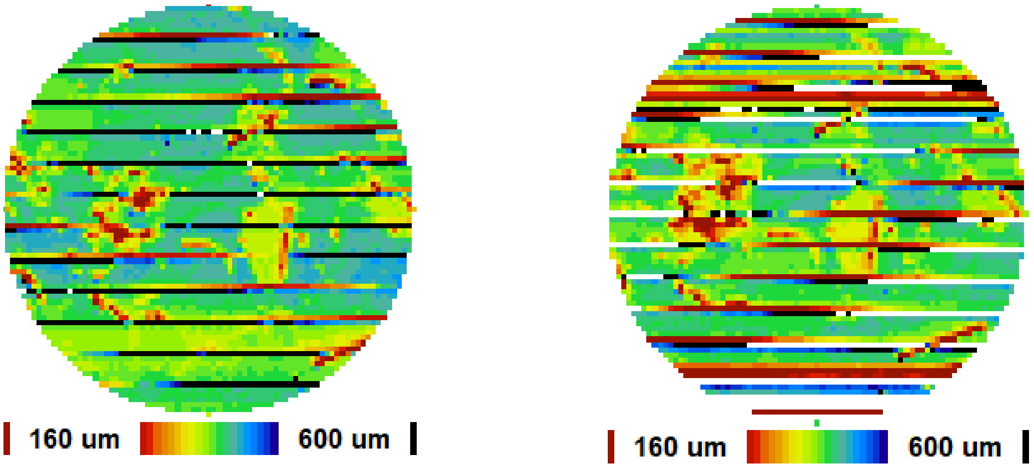

451 µm **393 µm**

Minority carrier lifetime (µs)

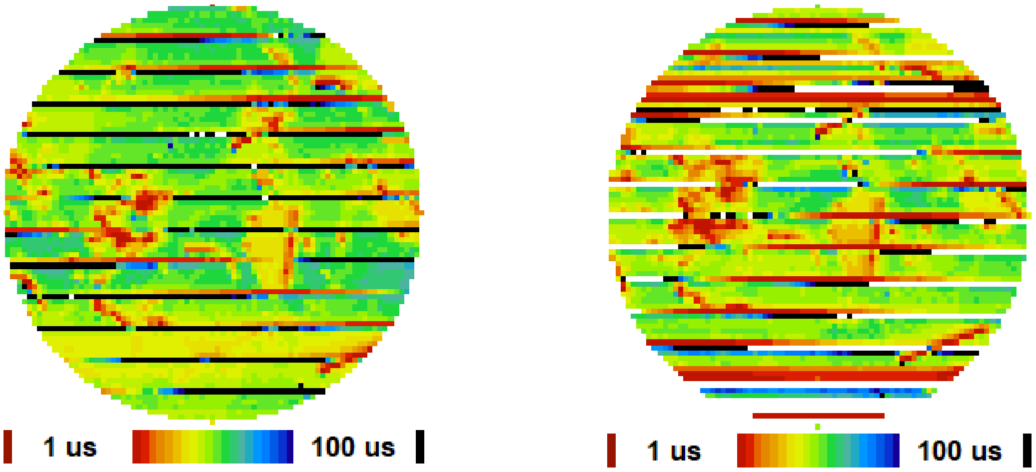

69 µs **55µs**

Figure 5: Minority carrier diffusion length and lifetime maps in the Mult crystalline solar cell before and after LID activation

4 Conclusion

This study presents a spatially resolved analysis of LID effects in multicrystalline silicon solar cells using wavelength-dependent LBIC, EQE, and IQE mapping. Our results demonstrate that LID leads to a homogeneous ~10–15% reduction in carrier collection efficiency across all wavelengths, with the most severe degradation observed in the bulk region (e.g., LD decreased from 451 μm to 393 μm, τ from 69 μs to 55 μs). The stronger decline in minority carrier lifetime (τ) compared to diffusion length (L) suggests the dominant role of Shockley-Read-Hall (SRH) recombination due to activated boron-oxygen (B-O) complexes. However, the ~40 μA LBIC reduction at 657 nm (shallow penetration) hints at additional degradation pathways, such as:

- Contact degradation: Prolonged illumination may exacerbate metal-grid-induced series resistance or contact recombination.
- Grain boundary effects: While bulk defects dominate, localized recombination at grain boundaries could contribute to spatial non-uniformity.
- Surface passivation instability: The slight but measurable drop in short-wavelength IQE suggests potential emitter or anti-reflection coating degradation.

These findings highlight that LID is not solely a bulk phenomenon but involves multi-scale interactions between bulk defects, surface/interface states, and metallization.

Acknowledgements

The authors thank the Tunisian Ministry of Higher Education and Scientific Research and The Japan International Cooperation Agency for the financial support.

References

1. H. Fischer, W. Pschunder, "Investigation of photon and thermal induced changes in silicon solar cells", Proc. 10th IEEE PVSC,." 1973.
2. M. Padmanabhan, K. Jhaveri, R. Sharma, P. K. Basu, S. Raj, J. Wong, and J. Li, "Light-induced degradation and regeneration of multicrystalline silicon Al-BSF and PERC solar cells," Physica Status Solidi-Rapid Research Letters, vol. 10, no. 12, pp. 874-881, Dec, 2016.
3. K. Bothe, R. Hezel, and J. Schmidt, "Understanding and reducing the boron-oxygen-related performance degradation in Czochralski silicon solar cells." pp. 223-228.
4. K. Bothe, and J. Schmidt, "Electronically activated boron-oxygen-related recombination centers in crystalline silicon," Journal of Applied Physics, vol. 99, no. 1, pp. 013701, 2006.
5. K. Bothe, and J. Schmidt, "Fast-forming boron-oxygen-related recombination center in crystalline silicon," Applied Physics Letters, vol. 87, no. 26, pp. 3, Dec, 2005.
6. D. Bredemeier, D. Walter, and J. Schmidt, "Light-induced lifetime degradation in high-performance multicrystalline silicon: Detailed kinetics of the defect activation," SOLAR ENERGY MATERIALS AND SOLAR CELLS, vol. 173, pp. 2-5, 2017-12-01, 2017.
7. M. Selinger, W. Kwapil, F. Schindler, K. Krauss, F. Fertig, B. Michl, W. Warta, and M. Schubert, "Spatially resolved analysis of light induced degradation of multicrystalline PERC solar cells." pp. 867-872.
8. M. Najjar, B. D. Rezgui, M. Bouaicha, O. Palais, B. Bessais, and S. Aouida, "Local activation of light-induced degradation in co-doped boron-phosphorus silicon: Evidence of defect diffusion phenomena," Materials Science in Semiconductor Processing, vol. 135, pp. 106104, 2021.
9. J. Schmidt, A. G. Aberle, and R. Hezel, "Investigation of carrier lifetime instabilities in Cz-grown silicon." pp. 13-18.
10. K. Bothe, R. Sinton, and J. Schmidt, "Fundamental boron–oxygen-related carrier lifetime limit in mono-and multicrystalline silicon," Progress in photovoltaics: Research and Applications, vol. 13, no.

4, pp. 287-296, 2005.

11. N. Harder, D. Neuhaus, P. Altermatt, and IEEE, "Discussion of recombination current mechanisms at grain boundaries in the bulk: A simplified model." pp. 491-494.
12. J. Käsewieter, F. Haase, M. Larrodé, and M. Köntges, "Cracks in solar cell metallization leading to module power loss under mechanical loads." pp. 469-477.
13. R. N. Hall, “Electron-hole recombination in germanium,” Physical review, vol. 87, no. 2, pp. 387, 1952.
14. T. Goudon, V. Miljanović, and C. Schmeiser, “On the Shockley–Read–Hall model: generation-recombination in semiconductors,” SIAM Journal on Applied Mathematics, vol. 67, no. 4, pp. 1183-1201, 2007.

-Funding :

The author thank the Tunisian Ministry of Higher Education and Scientific Research and the Japan International Cooperation Agency for the financial support.

-Data availability :

Data are avaible upon reasonable request